

Geophysical detection and structural characterization of discontinuities in rock slopes

(J. Deparis, D. Jongmans, S. Garambois, C. Levy, L. Baillet and O. Méric)

ABSTRACT

The stability of a potentially unstable rock mass strongly depends on the discontinuity pattern and the face topography. Basic geological analysis could provide useful structural information but suffers from the lack of information on discontinuities at depth. Of major importance is the persistence of discontinuities inside the mass. Several geophysical methods (seismic, electric and electromagnetic) are available to address this problem, differing in sensitivity, resolution and depth penetration.

The purpose of the chapter is to present the common structural and geophysical methods for characterizing the rock mass. Section 2 is dedicated to a review of the main geophysical parameters and the properties of the main geophysical methods, as well as their possibilities and limitations for discontinuity detection and characterization. In section 3, applications of the aforementioned methods are shown for three limestone cliff sites located around Grenoble (French Alps), exhibiting different geometrical and geotechnical features.

1 Introduction

Rock falls pose critical problems to risk management in mountain areas. Difficulty of prediction results from the phenomenon suddenness, the lack of identified reliable precursors, the poor information on the internal structure of the rock mass and the multiplicity of triggering factors (freeze thaw cycles, earthquakes, human activities, water infiltration..) ([FRA 06]). Rock mass stability assessment requires detailed investigations of the discontinuity pattern and of the 3D geometry of the potential unstable block ([HOE 81]).

In the context of rock cliffs, three types of investigations can be performed with this purpose:

1. Geological and structural observations made on the cliff face and on the plateau, including in open fractures when access is possible.
2. Remote sensing measurements (mainly photogrammetry and scan laser) which allow a digital surface model of the cliff to be obtained.
3. Geophysical experiments conducted on the plateau and/or on the cliff face.

The remote sensing techniques and their applications for monitoring rock slopes are described in the chapter 2 of this book and will not be detailed further. This chapter focalized on the description of the useful geophysical methods in this context, which allow the mass fracture pattern to be delineated from measurements on the plateau and/or on the cliff face. A review of the different parameters and their sensitivity is first reviewed followed by case studies conducted in various cliff faces located around the Grenoble area.

2 Geophysical parameters and methods

2.1 Introduction

Geophysical methods have been increasingly used for slope investigation (for a review see, [JON 07]). They are based on the field acquisition of physical measurements from which physical parameters can be deduced, generally through an inversion or imagery process. The measured data and corresponding parameters are summarized in Table 1 for the main geophysical methods (seismic, electrical, gravimetry, magnetism, electromagnetism, radar). It is beyond the scope of this paper to detail the methods that are described in general books ([REY 97], [TEL 90], [SHA 97], [KEA 02]). Compared to geotechnical techniques, geophysical methods offer the advantages to be quick, non-invasive and deployable on slopes, as well as to investigate a large volume of material and to provide 2D or 3D images ([JON 07]). On the other hand, contrary to geotechnical techniques, they suffer the following drawbacks: i) when measurements are made at the surface, their resolution decreases with depth; ii) the solution is generally non-unique for a given data set except for reflection-based methods, and iii) they provide physical parameters instead of geological or geotechnical properties. This list outlines the complementarities between the two families of investigation techniques.

The geophysical methods to apply have to be adequately selected for the problem to solve. [MCC 90] identified four factors to consider for designing of a geophysical survey: the existence of a geophysical contrast corresponding to the campaign target (e.g., the limit of the sliding mass), the penetration depth and the resolution (ability of the method to detect a body of a given size or thickness at the desired depth), the quality of the geophysical signal (noise perturbations) and the necessity to calibrate the geophysical results by geotechnical and geological data. This often requires that preliminary tests are made before designing a geophysical survey.

Method	Measurement	Physical parameter
Seismic	Propagation time	Wave velocity
Electrical	Electrical potential	Electrical resistivity
Gravimetry	Gravitational acceleration	Density
Magnetism	Magnetic field	Magnetic susceptibility

Electromagnetism	Electromagnetic field	Electrical resistivity
Radar	Propagation time	Dielectric constant

Table 1: Main geophysical methods, corresponding data and derived parameters.

In the context of rock stability assessment, the two principal objectives of geophysical experiments are to characterize the fracturing pattern inside the rock mass and to delineate the prone-to-fall block geometry. In the context of a cliff or high slope geometry, measurements can be performed on the top (plateau) or on the cliff face (Figure 1). Geophysical investigation on the plateau may provide valuable information about the continuity of outcropping structures (fractures, faults) or the rock quality ([DUS 03], [BUS 06], [HEI 06]). However, the investigation depth could be low compared to the cliff height and generally the method resolution decreases with depth. When possible, the use of GPR on the cliff face was found to be the most valuable tool in terms of resolution for investigating a rock mass ([DUS 03], [ROC 06], [JEA 06], [DEP 07], [DEP 08]). The main two limitations of GPR for cliff investigation are safety requirements for abseiling and the penetration depth which can be lowered by the rock low electrical resistivity values.

In the following sub-sections (2.2 to 2.5) the main physical parameters and the associated methods which can be used for rock fall investigation are described. The first three geophysical parameters (seismic velocity, electrical resistivity and dielectric permittivity) are common properties used in many applications in engineering and environmental geology ([REY 97]). On the contrary, the resonance frequency, which is derived from seismic noise tests records, is a mechanical parameter that has been rarely used for rock fall hazard assessment but originally for seismic site effect assessment.

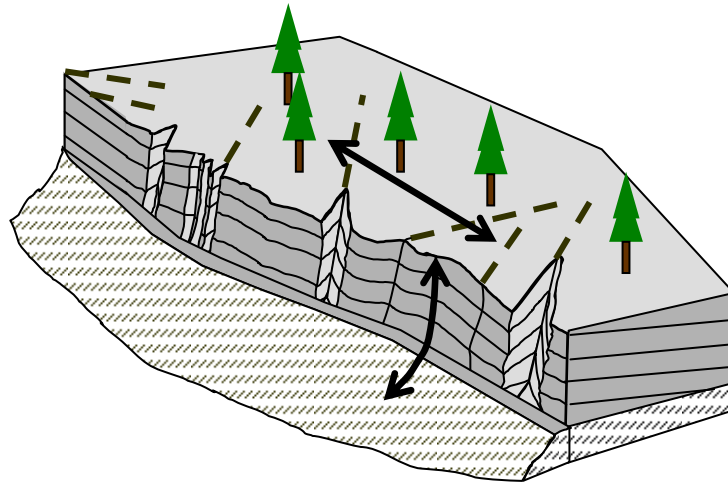


Figure 1. Cliff geometry showing bedded limestone overlying a marl layer with the location of potential geophysical profiles (double arrows) on the plateau or on the cliff face. Fracturing is highlighted with dotted lines.

2.2 Seismic velocity

3.1.1. Background

When applying a local stress on a material (with a seismic source for example), a resulting elastic strain propagates under seismic wave energy. Depending on the seismic source considered, two types of volume waves are generated, i.e., compression-dilatation waves (P waves) and shear waves (S waves). As P waves generate a volume change without any rotation of the material particles, particles displacements occur within the propagation direction. For S waves, particles movement is located in a plan perpendicular to the wave propagation direction. In any seismic survey, the main parameter that may be easily quantified is the seismic velocity distribution. It may be assess with a certain resolution, which depends on the seismic method used (reflection, refraction, tomography), on the seismic source (frequency content) and the source-receiver configuration. When considering an elastic material, the velocities associated to the P and S waves can be expressed as a function of elastic parameters:

$$V_p = \sqrt{\frac{\lambda + 2\mu}{\rho}} \quad \text{and} \quad V_s = \sqrt{\frac{\mu}{\rho}} \quad [1]$$

where λ and μ are the Lamé coefficient and ρ is the volume mass of the material. It is clear from this relation that P wave velocity (V_p) is always greater than S wave velocity (V_s).

Presence of heterogeneities within a rock mass will modify the velocity of the same un-weathered mass. For example, the presence of fractures or faults will decrease the velocities, the amount of decreasing depending on their scale, their properties (filling, aperture) and their amount. Of course, if the filling is full of water ($V_p=1500$ m/s), the decreasing will be lower than if the fractures are filled with air ($V_p=300$ m/s). Velocity sensitivity to fractures and the resulting anisotropy has been increasingly studied for reservoir purposes by oil companies but seldom studied in the context rock engineering (see [MAV 95] for a detailed analysis). The 2D and 3D seismic tomography provide a useful tool to characterize unstable slope. [HEI 06] produce a 3D seismic tomography which reveals the presence of a very low P wave of 500-2700m/s velocity in a huge volume compare to the 5400 m/s velocity of intact rock. The authors explain that values by the presence of 17% of volume of air filling voids due to ubiquitous dry crack, fracture zone and fault.

Besides volume waves, the presence of the free surface will generate surface waves, whose analyses of their dispersion characteristics can provide a quantitative depth profile of V_s after an inversion process [REY 97].

Seismic methods

Among the numerous active seismic methods available for imaging purposes, high resolution seismic reflection has been seldom used for rock fall problems, mainly because this method requires a bigger effort to deploy the geophone layouts, particularly in the conditions of rugged topography. Also, the success of shallow seismic reflection requires a good signal to noise ratio and the recording of high frequency waves to reach the desired resolution. These two conditions may be difficult to fulfill on rock masses as the ground may be strongly disturbed and heterogeneous. Also, the GPR method can fulfill resolution and penetration conditions with less effort in resistive rocks.

Other active seismic methods have been poorly applied to near-vertical cliffs or high natural rock slopes ([HAC 00]), mainly due to the practical difficulties of performing tests on such sites. Travel-time analyses as seismic refraction (Figure 2) are simple to conduct if all source and receivers are located on the plateau. However, cross-hole tomography has been the most popular method, tomography surveys conducted with all sources and receivers located on the ground surface are increasingly used ([LAN 98]; [JON 00]). On steep slopes, seismic imaging was applied by [ZOU 01] in a quarry to investigate the blast-induced fracture in rock mass between the horizontal bench and the vertical wall, and by [JON 00] to assess the stability along railway slopes affected by a rock slide. [DUS 03] proposed a

seismic tomography, which investigated a triangular zone, 34 m by 15 m, with sources and geophones located both on the plateau and on the cliff face (Figure 3).

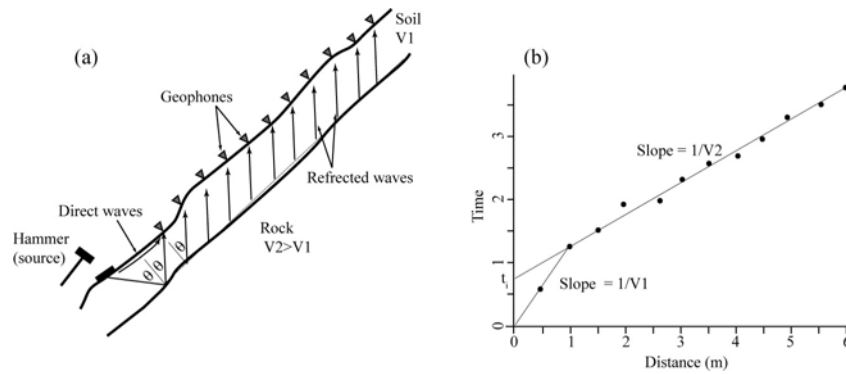


Figure 2. Seismic refraction method. (a) Ray paths. (b) First arrival time versus offset curve [HAC 00].

It provided a global model of rock properties, through an image of seismic velocity which decreases in areas where a large amount of fractures are present. The measured images, which show strong velocity gradients (800 to 3500 m/s over a few metres), are very similar to those obtained with synthetic models in which vertical fractures give rise to low-velocity zones. However, smoothing of the inversion process and poor resolution due to the sources-receivers configuration, significantly modify the shape of the anomalies.

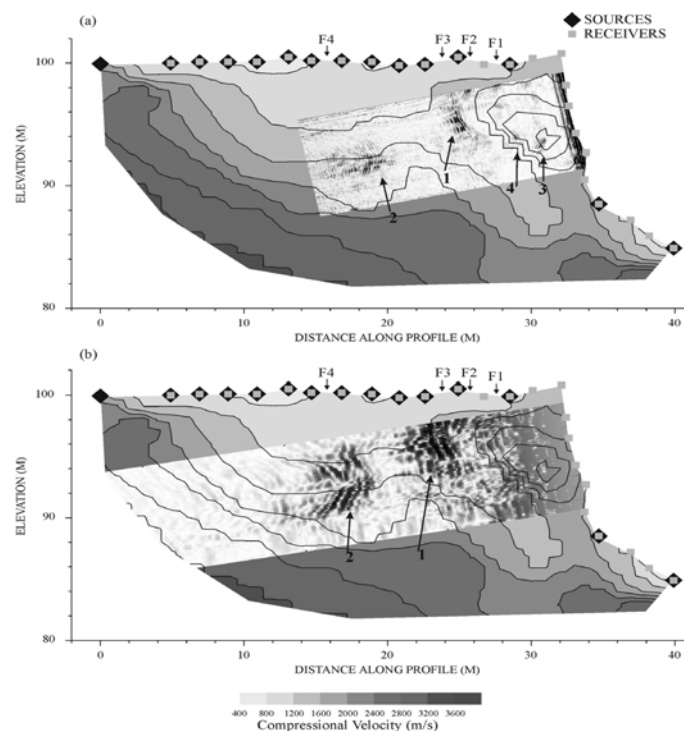


Figure 3. Superimposition of a P-wave tomography image with GPR reflection data ([DUS 03])

Seismic anisotropy

The rocks are often characterized by anisotropy, which may be due by the preferred orientation of minerals (foliation in metamorphic rocks), the discontinuities such as faults, fractures and bedding planes and other rock joints. This anisotropy result by the fact that the rock formation and deformation properties could be different in function of direction (orientated minerals or sets of orientated discontinuities). For example, a rock affected by one set of discontinuities present higher seismic velocities parallel to these discontinuities, and lower seismic velocities perpendicular to these discontinuities ([HAC 00]). Figure 4 shows a so-called seismic refraction fan shooting and the resulting seismic velocities in function of direction. At this scale, the difference in seismic velocities can reach over 50% depending on the direction of the profile.

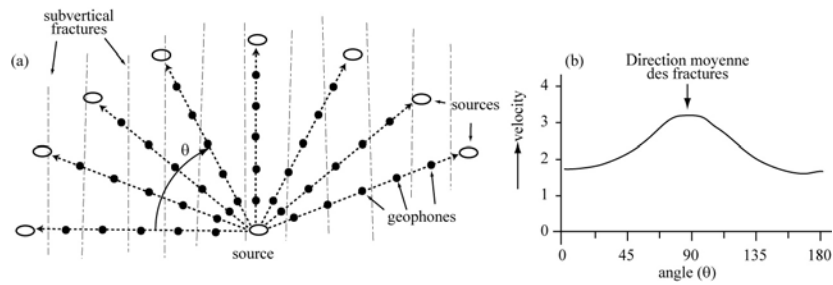


Figure 4. Seismic velocity anisotropy. (a) Source-receiver Star configuration. (b) Resulting seismic velocities as a function of profile azimuth compares to discontinuities [HAC 00].

2.3 Electrical resistivity

Electrical conductivity [S/m], usually denoted σ , is the physical property which determines the aptitude of the material to allow to the passage of electrical current. The conductivity is the ohmic conductance of a cylinder of unit section A and length L can be written $\sigma=I.L/(V.A)$, where V and I are the potential difference across the cylinder and the current through it. In geophysics, the inverse of the conductivity, i.e. the resistivity is more commonly used. Electrical resistivity of rock exhibits a broad band, ranging from $1.6 \times 10^{-8} \Omega.m$ for native silver to $10^{16} \Omega.m$ for pure sulphur.

Electrical current may propagate in the soil according to three mechanisms: i) electronic (ohmic) conduction which allow electrons to move rapidly, ii) dielectric conduction, which occurs when an transitory electric field is applied in low conduction materials and iii) electrolytic conduction, where the current is diffuse by slow ions movements present within an electrolyte. In this case, the electrical conductivity of the material depends upon the mobility and charge of ions and the electrolyte amount present within the material.

With the notable exception of clays or very fine sediments where surface conduction dominates by a process of proton exchange, the rock conduction is of electrolytic type in the majority of cases in earth materials. In this case, the electrical conductivity is controlled by the presence of discontinuity and the rock matrix type. [ARC 42] developed an empirical formula for the effective resistivity of saturated rock formation (ρ_r) which depends of the porosity (ϕ), the volume fraction of pores filled with water (s), and the water resistivity (ρ_w).

$$\rho_r = a^{-m} s^{-n} \rho_w \quad [2]$$

where A , m and n are constant and $0.5 \leq a \leq 2.5$; $1.3 \leq m \leq 2.5$ and $n \approx 2$

The solid conductivity (electronic and dielectric conduction) is significant for certain mineral deposits (graphite, gold, silver ...), certain oxides (magnetite ...) and sulphides (pyrite ...).

Electrical measurement

Electrical resistivity methods are commonly used in geophysical exploration for various applications, ranging from mine exploration to hydrological and environmental purposes, with a recent increase of time monitoring applications to study various phenomena. The goal of electrical prospecting is to determine the distribution of electrical resistivity in the ground surface. For this, a known current I

is injected between two electrodes A and B and the generated potential differences is measured between two other electrodes M and N (Figure 5).

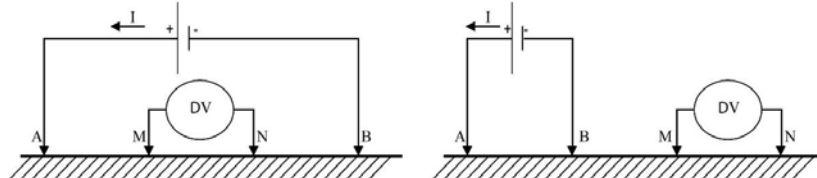


Figure 5. Quadripole configuration: (a) Wenner alpha ($AM=MN=NB$) or Wenner Schlumberger ($AM \neq MN \neq NB$) and (b) dipole-dipole.

With the potential difference between M and N electrode and the intensity of the current, the ground apparent resistivity is:

$$\rho_a = K \frac{\Delta V}{I} \quad [3]$$

where K is the geometrical factor, and depends only of the distance between the four electrodes:

$$K = 2\pi \left(\frac{1}{AM} - \frac{1}{BM} - \frac{1}{AN} + \frac{1}{BN} \right)^{-1} \quad [4]$$

Various electrode configurations have been developed (Wenner, Schlumberger, dipole-dipole), which differ by their depth penetration, sensitivity and resolution. The depth penetration roughly ranges between the value $AB/6$ for the Wenner configuration and the quarter of the spacing of the two away electrodes for the dipole-dipole configuration. The resolution is function of the distance between the electrode, of the configuration type and of the resistivity distribution and the investigate depth. The Wenner configuration is recommended to image horizontal structure, Wenner-Schlumberger is recommended both for vertical and horizontal structure and Dipole-Dipole configuration is recommended especially for vertical structures.

In the case of homogeneous and isotropic formations, the obtained apparent resistivity is the true resistivity. On the other hand, when the ground is heterogeneous, the apparent resistivity is function of the true resistivity of the various formations encountered and of the dimension of the array used. Indeed, measurement represents a value, which integrates the resistivity of a certain volume of the earth. To retrieve the true resistivity distribution of the ground, an inversion

process has to be applied to the data. In the past, 1D sounding profiles were acquired, consisting in a resistivity curve versus $AB/2$. In this case, the inversion process was simply made by try and error tests, assuming a 1D distribution of the resistivity, only varying vertically. Of course, this assumption was not valid as soon as more complex structures were investigated.

Electrical tomography

In order to take into account the lateral and vertical resistivity variations, electrical resistivity tomography (ERT) was developed within the past 20 years. It consists in deploying a large number of electrodes, which are simultaneously connected via a multichannel cable to a resistivity-meter. It enables to automatically switch the electrode spacing and position according to a previously defined acquisition configuration and to obtain a 2D or 3D distribution of apparent resistivity.

The inversion process is the crucial step in this technique [REY 97], which must be carefully scrutinized. For example, non-uniqueness is the cause of various misinterpretation. A conductive bed located between two or more resistive materials, essentially exhibits its "longitudinal conductance" thickness divided by the resistivity (h/ρ). Any change of resistivity and thickness, which keeps constant the ratio will provide the same apparent resistivity.

Fracture in limestone can be highlighted on electrical tomography images by conductive anomalies when water or clays are filling the material or by resistive anomalies in case of air filling.

Figure 6 show an example of acquisition and process tomography acquire on the top of the plateau near a vertical cliff ([DEP 08]). Apparent resistivity pseudosection is presented in Figure 6a. Inversion process which generally based on smoothness constrained least-squares method ([LOK 96]) calculated the true resistivity (Figure 6c). Root Mean Square (RMS) error is obtained by the comparison between calculated apparent resistivity model (Figure 6b) obtained with the inversed pseudosection and field data. The mean resistivity of the rock mass varies between a few hundreds of Ohm.m and 1500 Ohm.m on the profiles. These relatively low values characterize a weathered limestone with marls ([REY 97]). A strong vertical resistive anomaly appears at a distance of 18 m. This anomaly corresponds to the open fracture observed on the plateau.

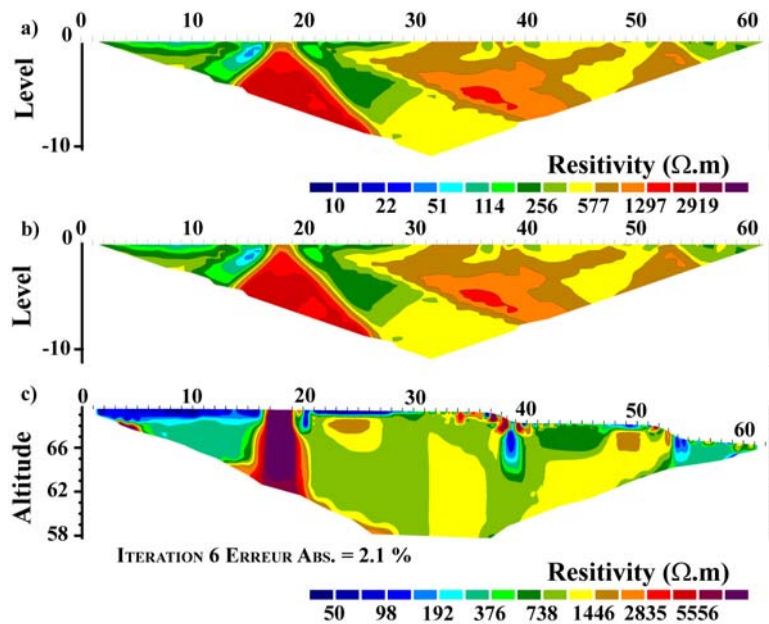


Figure 6. Electrical tomography acquired on the plateau near vertical cliff. a) Apparent resistivity data, b) calculated raw resistivity and c) inverted resistivity section.

For discontinuity imaging, [HEI 10] present electrical results obtained on a large Rockslide. They associated low resistive values with the presence of a water-filled tension fracture. [NOR 09] use 3D electrical resistive tomography and geotechnical data to estimate the geometrical extent of the basal sliding surface(s) on which the slope failure may potentially occur. With these results, the author presents three scenarios for different geometries of the sliding surface and computed the potential investigated volumes of rock for each scenario.

2.4 Dielectrical permittivity

Electromagnetic wave propagation is controlled by coupled Maxwell's equations and depends on frequency and on macroscopic constitutive properties, which describe the material's response to electromagnetic fields, i.e., electrical conductivity, dielectrical permittivity and magnetic permeability ([SAN 01]). Electrical conductivity (σ) describes conduction current, i.e., free charge movement when an electric current is applied to the material. It governs electromagnetic attenuation due to energy loss. Dielectrical permittivity (ϵ) characterizes displacement of charge constrained in a material structure to the presence of an electric field (energy storage). Its real part is directly related to EM wave velocity. Magnetic permeability (μ), which is defined as the ratio of flux density to magnetic field strength, denotes the degree of magnetization that a material obtains in response to an applied magnetic field. In a large range of rocks and soils, this value can be taken at the vacuum permeability. All these quantities are in general complex and highly dispersive.

Depending on frequency, conductivity and dielectrical permittivity, the EM fields may be either diffusive (low frequencies, high conductivity) or propagating (high frequency and dielectric permittivity). In the range of Ground Penetrating Radar, where microwave are used, radar wave propagation range permits to image the subsurface. In this case, EM velocity v directly depends on the relative permittivity κ ($\kappa = \epsilon_r / \epsilon_0$, where $\epsilon_0 = 8.85 \times 10^{-12}$ F/m and ϵ_r denotes the real part of ϵ): $v = c / (\kappa^{1/2})$, c being the velocity of the vacuum (0.3 m/ns). It must be noted that as the relative permittivity of water equals 81 at 0°C and equals 1 for vacuum, permittivity of any rock and soil formation is strongly sensitive to the relative proportion of air and water.

GPR imagery follows seismic reflection principles. Basically, a transmitting antenna (Tx) emits a transitory frequency-dependant electromagnetic pulses which penetrates within the material and is reflected and scattered when crossing any material exhibiting contrasts in any of the constitutive properties mentioned here above. Scattering appears when the typical dimension of the object is lower than the incident wavelength. The resulting signal is recorded as a function of propagation time using a receiving antenna, which is constantly located near the source. By displacing the antennas with a constant offset, one obtain a classical time single-offset image, which must be corrected from dynamic effects (Normal Move Out effects), from geometrical distortions via a migration process and must converted into depth sections. Depending on the desired resolution (which equals the wavelength divided by 4 following Rayleigh's criteria) and penetration depth, the

choice of the frequency of the antennas is a crucial step, ranging from a few MHz in very resistive material (cold ice) to a few GHz for very superficial and geotechnical purposes. In very high resistive materials (ice, un-weathered rocks), depth penetration can reach several tens of meters at 100 MHz (more on glaciers) with a vertical resolution of 25 cm. For these reasons, GPR has been increasingly used in the context of fracture detection since ten years, the media of interest being in general resistive.

For fracture imaging and characterization, reflected waves are used using two acquisition configurations: i) the single-offset aforementioned mode for imaging and ii) a Common Mid-Point profile (CMP), dedicated to estimate variations of the electromagnetic velocity as a function of depth. Indeed, velocity characterization is crucial to correctly apply the needed corrections to the raw data (dynamic correction, migration, time to depth conversion) but can also permit to characterize the material. A CMP profile is obtained by varying the radar antenna spacing across a central location until about the depth of investigation is reached. It allows analyzing the Normal move Out of the reflected hyperbola events as a function of time.

In the past decade, GPR has been used extensively for fault and fracture mapping in 2D ([BEN 95]; [TOS 95]; [STE 95]; [DEM 01]; [RAS 03]) and in 3D ([GRA 96]; [PIP 03]; [GRA 05]). [PET 96] and [PIP 03] showed, from 2D and 3D radar measurements, that discontinuities filled with clay, water or air are clearly detectable when an appropriate signal frequency is used. Considering these results, GPR experiments conducted along vertical cliffs have emerged in the last couple of years and showed that GPR profiles conducted on the cliff face yielded the best results in terms of penetration and resolution and provided the geometry and continuity of the major open joints. [JEA 06] studied different acquisition configurations (reflection, tomography) on a limestone cliff, which did not present any rock fall risk. They notably presented 100 MHz GPR reflection profiles, which reached a penetration depth of 20 m with a vertical resolution of 25 cm. They showed that location and orientation of several reflectors coincide with the fractures observed from the surface. [ROC 06] acquired 3D GPR data, which were combined with photogrammetric data to derive a quantitative 3D interpretation in terms of discontinuities. They notably imaged a major fracture, which presents an extent of 350 m² partly at the surface of the rock wall. [DEP 07] illustrates, with a case study located in the Gorges de la Bourne (French Alps), how multifrequency GPR measurements taken on a potentially unstable rock slab overhanging a road, whose interpretation was validated by independent measurements, can help hazard assessment and mitigation decision.

GPR imagery of dielectric contrasts provides geometrical information of major discontinuities and of their continuity, whose amplitude and waveform depends on

fracture properties. Figure 7 shows on a synthetic case the variations of reflection on a fracture, whose ratio aperture/wavelength (d/λ_f) is varying.

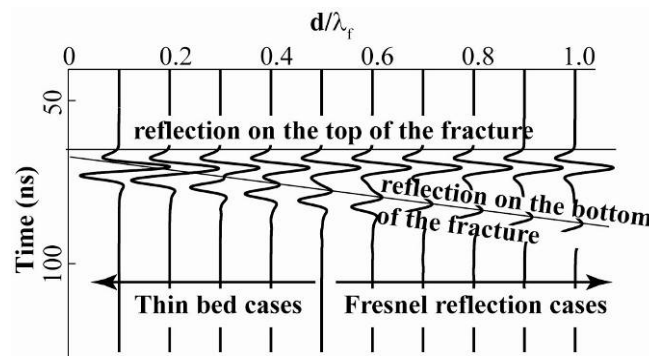


Figure 7. Synthetic reflected GPR signals originated from a fracture as a function of the aperture/wavelength ratio (after [DEP 10]).

If these discontinuities are largely opened (compared to the wavelength), two reflections can be detected, coming from both sides of the fractures, as displayed when the ratio aperture/wavelength (d/λ_f) is greater than 0.5. In this case, Common Middle Point data are able to provide quantitative information on dielectric properties of the filling material and consequently on aperture. When the ratio is decreasing, first only a single reflection will be detected, preventing any direct characterization of the fracture properties. Also, if the fracture appears to be very thin, no reflection will be detected and consequently, the GPR images must be carefully interpreted as a maximal linear percentage of rock bridges as too thin fractures are not being detected.

In the case of a thin layer (ratio lower than 0.5), the reflection coefficient at the interface does not obey anymore to the classical Fresnel equation, but is due to interferences between reflections coming from both sides of the thin-bed. It presents a more complex equation ([DEP 10]), which is controlled by complex permittivity dielectric contrasts and aperture ([ANN 02]), and shows large frequency and angular variations. From synthetic and field data, [LAN 00] showed that water-filled fractures generate larger reflected GPR signals than those filled with air. Previously, [PET 96] have also shown that a limestone/limestone joint contact was impossible to detect, unless it was filled with clays or calcite. From these observations, [GRE 04] compared the spectral ratio between measured reflected wavelets and a reference wavelet for the case of thin-bed reflectors to estimate the dispersive dielectric permittivity of the reflectors and their apertures. This frequency-sensitive approach was only applied to constant offset sections and needed a reference signal, hard to obtain in real cases. Besides this dispersive approach, [BRA 06] analyzed Amplitude Versus Offset (AVO) curves using an analytical solution of the thin-bed reflectivity,

and successfully applied their modelling to two case studies dealing with Nonaqueous Phase Liquids (NAPL) contaminated zones. However, the authors did not account for the dispersive properties of constitutive parameters. To go further, [DEP 09] and [DEP 10] presented an original approach which aimed to combine dispersion and AVO information in order to fully describe thin layer and the surrounding material. For this, they proposed an inversion algorithm which consists to invert dispersion properties of Amplitude and Phase versus offset curves, which are retrieved from the reflection attributes acquired with a CMP configuration. Reflectivity sensitivity is provided on Figure 8.

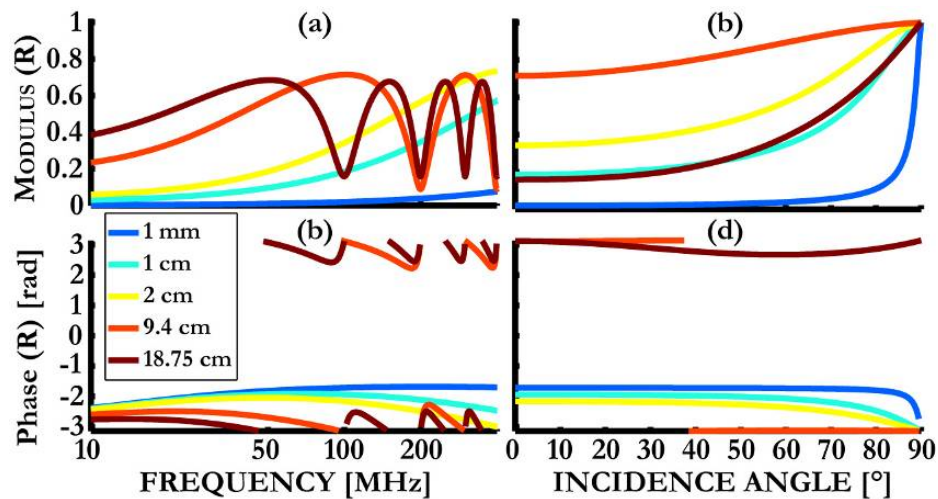


Figure 8. Phase and modulus of a reflected event due to the presence of a thin-layer presenting various apertures as a function of frequency (left) and incidence angle (right).

This approach, which has been successfully applied to CMP data acquired along a vertical cliff for fracture characterization, can be enlarged to all contact zones, provided that the material is homogeneous. In future, it must be applied to more complex media, and particularly by using and inverting the GPR full-waveform, both in 2D and in 3D.

2.5 Resonance frequency

The idea of using seismic resonance (or natural) frequency for rock fall hazard assessment is based on previous results obtained in civil engineering. Indeed, [CLI 06] processed continuous ambient vibration records to study the drop in the resonance frequencies of buildings, resulting from a decrease in system stiffness with the progressive damaging during earthquakes. Similarly, natural frequencies of a rock column, which should vary with the stiffness of the contact to the rock mass, could be used for evaluating the degree of coupling of a prone-to-fall column to the rock massif [DEP 07b]. After a brief summary about the theoretical dynamic response of a complex structure, we discuss the characteristics of the ambient seismic noise and its application for assessing the dynamic behavior of geological structures like prone-to-fall column and spurs. The potentiality of the technique is illustrated on a synthetic case simulating the Chamousset rock fall, which is presented in section 3.3.

Dynamic response of a structure

The classical form of the differential equations of motion for a complex structure is:

$$M \ddot{x}(t) + C \dot{x}(t) + K x(t) = P(t) \quad [5]$$

where M , C , K are the mass, viscous damping and stiffness $N \times N$ matrices, respectively, P and x are the applied forces and the displacement $N \times 1$ vectors. Considering proportional damping ($C = \alpha_m M + \alpha_k K$), the Eigen solution at the full space of the physical model is:

$$M^{-1} K \phi_j = \omega_j^2 \phi_j \quad \text{for } j=1, N \quad [6]$$

In this equation, the N circular frequencies ω_j approximations are the square roots of the eigenvalues of $M^{-1} K$ and the N modes shape (or modes of vibration) ϕ_j are developed from their eigenvectors. Since M et K are symmetric, the N circular frequencies are real values $\omega_1 \leq \omega_2 \leq \dots \leq \omega_N$.

Once the mode shapes are available, their orthogonality property allows the linear response $x(t)$ of the structure to be constructed as the response of N single degree of freedom systems. Using the transformation from physical space to modal

space $x(t) = \sum_{j=1}^N \phi_j \alpha_j(t)$ [7] where α_j is the scalar mode participation, the equation of motion corresponding to the j^{th} modes becomes:

$$m_j \ddot{\alpha}_j(t) + c_j \dot{\alpha}_j(t) + k_j \alpha_j(t) = p_j(t) = \phi_j^T P(t) \quad [8]$$

where $m_j = \phi_j^T M \phi_j$, $k_j = \phi_j^T K \phi_j$, $c_j = \phi_j^T C \phi_j$ and p_j is the load projected onto this mode.

The finite element method is widely used for predicting the response of structures with complex geometries and boundary conditions, considered as N degrees of freedom with $N \rightarrow \infty$.

Ambient vibration tests

Ambient vibration testing has recently become the main experimental method available for assessing the dynamic behavior of full-scale structures. At low frequencies (<1Hz), ground noise is generated by ocean waves ([BON 06]) and at high frequencies by wind (about 0.5 Hz up to about 15 to 60 Hz, [YOU 96]) and man-made sources (road and rail traffic, industries, >2-4 Hz, [HAV 04]).

The ambient noise can be viewed as non-periodic excitation acting on the structure. A periodic version of the given load is constructed by defining a length T_0 for the time windows. As the ambient noise amplitude is relatively small, long time windows have to be recorded to ensure that all the modes of interest are sufficiently excited. Duration should be at least 1000 to 2000 times the period of the structure's fundamental mode ([CAN 05]).

The seismic excitation is then expressed as a sum of all the harmonic terms of its Fourier series:

$$p_i(t) = a_0 + \sum_{n=1}^{+\infty} a_n \cos n\omega_0 t + \sum_{n=1}^{+\infty} b_n \sin n\omega_0 t = \sum_{n=-\infty}^{+\infty} c_n e^{in\omega_0 t} \quad [9]$$

where $c_n = \frac{1}{T_0} \int_{-T_0/2}^{T_0/2} p_i(t) e^{-in\omega_0 t} dt$, a_n, b_n are constant coefficients to be determined and $\omega_0 = 2\pi/T_0 = 2\pi f_0$.

Although the input forces are unknown, the seismic excitation has to approximately satisfy the characteristics of a white noise, i.e. to have a flat spectrum around the resonance frequency that must be estimated. Providing that the structure is linear, the steady state response $\alpha_{j(t)}$ measured for each modal degree of freedom to a harmonic load component is calculated separately. These responses are then stacked to obtain the total response (principle of superposition). As the initial transient response associated with the free vibration decays rapidly with time for damped structure, the above solution represents the finally established response.

The solution to the N single-degree-of-freedom equations (equation [8]) to a periodic load (equation [9]) is given by ([HUM 90]):

$$\alpha_{j=1,N}(t) = \sum_{n=-\infty}^{+\infty} c_n H_j(n\omega_0) e^{in\omega_0 t} \quad [10]$$

$$\text{where } H_j(n\omega_0) = \frac{1}{m_j(\omega_j^2 + ic_j n\omega_0/m_j - n^2\omega_0^2)}$$

The total steady state response in physical coordinates (equation [7]) is then obtained by superimposing the modal responses (equation [10]). Considering zero damping ($c_j=0$) for sake of simplicity, structure resonance occurs when the excitation of circular frequency $n\omega_0$ coincides with the circular frequencies $\omega_{j=1,N}$ of the structure. The structures frequencies $f_{j=1,N}$ excited by the seismic noise (white noise assumption) will be clearly visible (extreme values) on a noise spectrum deduced from recorded seismic signal.

However, the higher modes identified through ambient vibration measurements could be less reliable if they are not excited sufficiently (REN 04]). In a rural environment (away from man-made noise), the noise level decreases at high frequencies (peak displacement of few nm at 1 Hz, two orders of magnitude lower beyond 10 Hz, [BRU 59] and [AKI 02]).

If the input excitation contains some dominant frequency components, they can be separated from the structure natural frequencies by computing spectral ratios between records acquired on and off the structure.

Numerical modelling of the Chamousset rock column

The use of the ambient seismic noise for deriving resonance frequencies is illustrated on a 2D synthetic case simulating the Chamousset rock column, which fell in November 2007 ([LEV 10]). A 2D explicit dynamic analysis of the column is achieved to mimic the evolution of the first column resonance frequency prior its collapse. The 2D column geometry (Figure 9) is derived from the Lidar data acquired before and after the fall (Figure 19, page 36).

Values of Young modulus and Poisson ratio for the structure were derived from the P and S wave velocities provided by available seismic profiles ([LEV 10]). The structure was modeled using 9245 quadrilateral finite elements. Rock bridges were set at the two zones along the scar (Figure 19, page 36), where fresh rupture was evidenced during abseiling ([LEV 10]). The remaining part of the interface is subjected to Coulomb friction ($\mu=0.7$) whenever in contact. The medium was permanently excited using white noise ([MAT 98]) sources placed on the surface of the mass and the column (see white stars in Figure 9a and b). Synthetic signals were computed at two nodes (Figure 9b) located on top of the rock mass (sensor 2) and of the column surface (sensor 1). The transient dynamic modeling simulated the progressive brittle failure of the rock bridges located in the upper part (from 268 m to 280 m in elevation) along the prone to be broken plane, considering 5 rupture stages (Figure 9b).

At the end of the 5 stages, the critical cohesion on the remaining rock bridges (white circles on Figure 9b) exceeded the initial cohesion and led to the column collapse.

The evolution of the column-to-mass spectral ratio for the five stages (sensor 1 in Figure 9b) is shown in Figure 10 for the horizontal components between 0 and 20 Hz. Spectra exhibit one predominant energy peak at a low frequency, which consistently decreases at each stage, from 5 Hz to 1.8 Hz. These values encompass the experimental peak frequencies (3.6 to 2.6 Hz), (Figure 20, page 37) which were interpreted as the lowest resonance frequency of the column.

A modal analysis has also been conducted to compute the first resonance frequency of the column during each stage (white dots on Figure 10) and the mode shape in the third stage (Figure 9c). These frequencies perfectly match the predominant peaks derived from the simulated ambient vibrations.

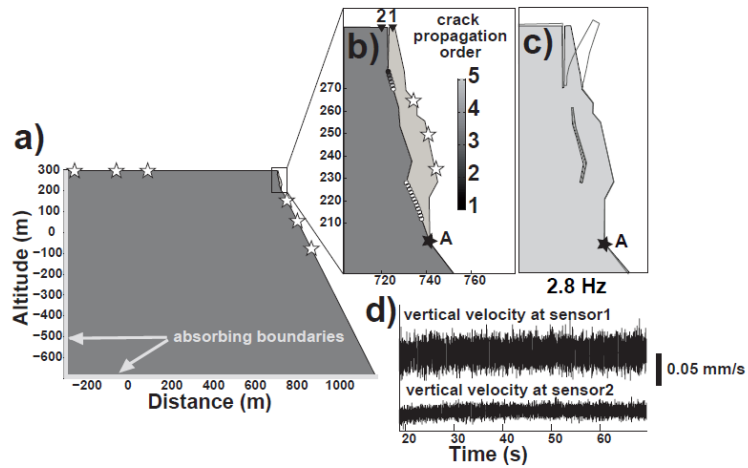


Figure 9. a) Geometry of the rock mass and of the column. White stars stand for seismic noise sources. b) Cross-section through the Chamousset column with the location of the two sensors (black triangles) and of the two zones of rock bridges along the scar. Filled circles correspond to rock bridges evolution. c) 1st mode shape ϕ_1 deduced from a 2D modal analysis during the third stage. d) synthetic noise seismograms at stage 1 on the column and on the mass.

These numerical results suggest that the evolution of lowest natural frequency f_1 , derived from ambient seismic noise records, could be a reliable precursor of rock falls at least in stiff rocks exhibiting rock bridges like limestone.

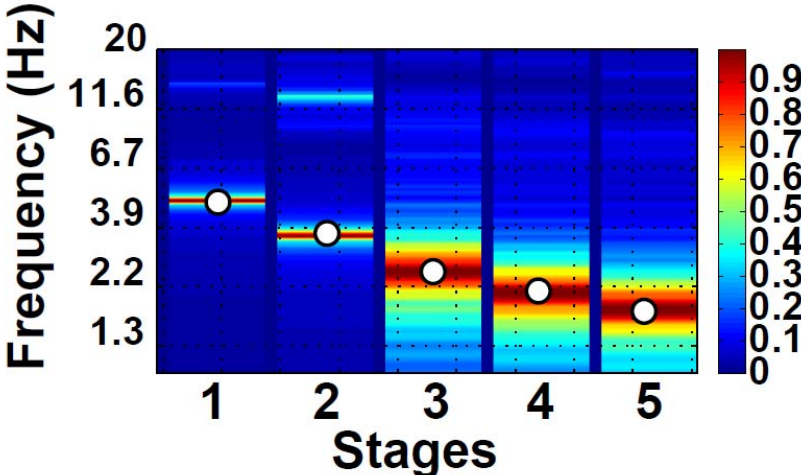


Figure 10. Normalized column-to-mass spectral ratio in the horizontal directions derived from the simulated ambient noise. White dots indicate the 1st frequency resonance obtain by modal analysis.

3 Applications

3.1 Introduction

This section presents real geophysical datasets derived from various methods dedicated to characterize the fracturing pattern on three cliff sites located in the French sub-alpine limestone Massifs of Vercors and Chartreuse: “Les Gorges de la Bourne” (Vercors massif), “le Ravin de l’Aiguille” (Chartreuse massif) and “Chamrousset” (Vercors massif) (Figure 11). On each site, geometrical and mechanical characteristics of the cliffs have led to adapt the investigation survey.

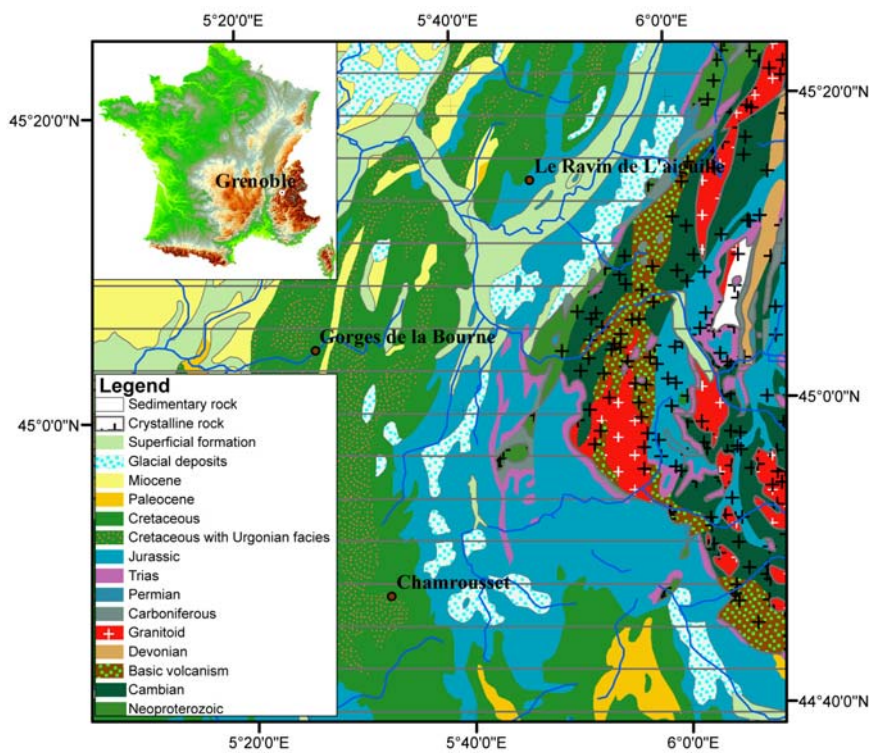


Figure 11. Location map of the three case studies displayed hereafter around Grenoble (Alps, France). cliff sites: Le Ravin de l’Aiguille, les Gorges de la Bourne and Chamrousset.

3.2 Plateau survey : Ravin de l'Aiguille

Geological context

The “Ravin de l’aiguille” site is located in the Chartreuse massif about 10 km north-est from Grenoble, at the top of the cliff 500 m high, which forming the eastern edge of the Chartreuse massif. The cliff is forming by a succession of upper and lower Tithonian limestone which dips to the northwest. Field observations allowed to identify three major discontinuities: (1) laminations joints (N210 ° / 20 ° W), (2) F_a families of fractures (N70 ° / 70 ° S) and (3) F_b (N130 °, subvertical).

The site “Le Ravin de l’Aiguille” is a 100 m wide and 170 m high tetrahedron, down pointed and limited by two large fractures F_a and F_b striking N65°E and N130°, respectively. The tetrahedron exhibits current signs of instability, with frequent rock falls. The potential unstable volume was originally estimated to $2 \cdot 10^5 \text{ m}^3$. Due to the danger of abseiling, GPR acquisition is impossible to perform on this cliff face and geophysical prospecting methods (seismic and electrical profiles) were applied on the plateau in order to delineate the internal limits and fractures of the unstable rock mass.

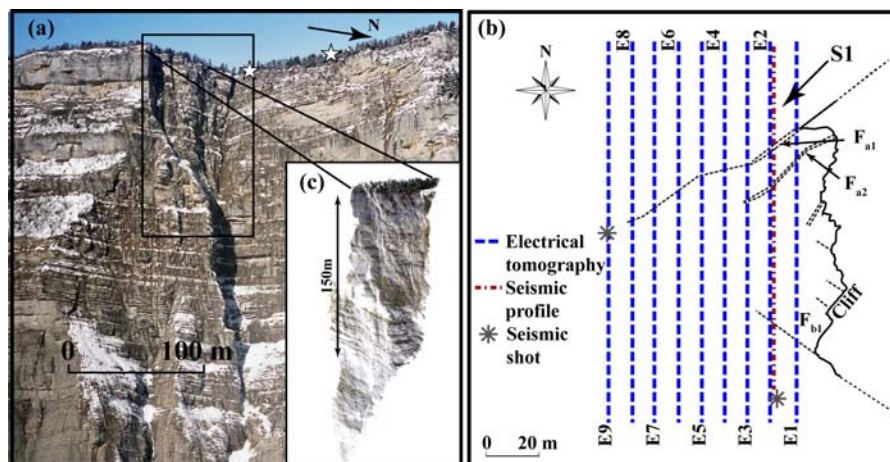


Figure 12. (a) Helicopter views of the Ravin de l’Aiguille site, (b) schematic surface maps showing the location of the main observed fractures and of the geophysical profiles and (c) dense digital surface models derived from Lidar acquisition.

Structural analysis of the cliff using solids images

Terrestrial laser scanning was made from two different locations in order to have the most complete as possible coverage of the cliff. Acquisitions points are located north of the cliff face (star on Figure 12a). The first one looked at the scarp with a very low incidence angle while the second one had an incidence of 30° in average. Figure 12c shows a view of the “Ravin de l’Aiguille” scarp from the first scanning point. The dots have a color computed from digital images of the site.

The process chain of the laser raw data was as follows:

- Orientation of each point cloud: we placed on the cliff high reflectivity targets that were easily distinguished in the point cloud. The location of these targets was measured in the field and used to transform the laser coordinates to geographical coordinates. After this step the point clouds were northerly and vertically oriented.
- Filtering of outliers for eliminating isolated points that are significantly far from the scarp.
- Filtering of points corresponding to the vegetation in order to keep only the points on the rock face itself.
- Co-registration of points clouds with the images of the sites. This step led to have solid images. All points of the clouds are re-projected in the images, allowing the field location of each pixel to be fixed,
- Triangulation of the point clouds. Each point cloud was triangulated independently in a spherical geometry, using only laser (azimuth, dip) coordinates ([ALB 04]). This processing chain results in a TIN (Triangular Irregular Network), a model of the site close to the real surface at a resolution of a few cm. The TIN was then mostly used for viewing in combination with the images of the site (Figure 12c)

A structural analysis was first performed on the accessible outcrops. The fractures were measured with a clinometers-compass and are shown in Figure 13a. A remote analysis (Figure 13b) was done using the solid images on which fracture planes were manually delimited. If the selected areas are planar, the best fit plane is computed. The selected fracture planes have a surface ranging between 10^{-1} m^2 to a few m^2 . Most of them correspond to fractures or to small faults. Comparison between both methods give similar results (Figure 13 a and b) although with slightly

different orientations. Due to the difficulty of measurement, the number of outcrop data is lower than the remote technique. The measurements also show two families of vertical fractures, $N65^{\circ}E \pm 15^{\circ}$ and $N140^{\circ}E \pm 20^{\circ}$, the orientation of which correspond to the ones of the two large fractures F_a and F_b limiting the tetrahedron, north and south respectively.

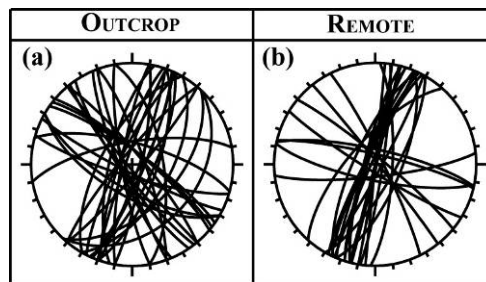


Figure 13. Stereographic projection (lower hemisphere) of the fracture planes measured at the “Ravin de l’aiguille”. The left column represent the data collected directly in the field while data remotely measured on the solid images are on the right.

Geophysical investigation

As the cliff face conditions do not allow abseiling, nine ERT profiles (labelled $E1$ to $E9$ in Figure 12b) and one seismic profile (SI) were conducted on the plateau (Figure 12b), parallel to the cliff face.

Electrical images (Figure 14a) exhibit resistivity values ranging from 1000 to more than 14000 $\Omega.m$. The dihedron affected by open fractures is characterized by high resistivity values of a few thousands $\Omega.m$ bounded by conductive zones (less than 400 $\Omega.m$). To the north, the narrow conductive zone coincides with the major fracture F_{a1} limiting the dihedron and filled with clay. This fracture is clearly mapped by the electrical profiles down to 20 m depth, particularly on the $E1$ to $E5$ profiles. To the south and in the middle, the resistivity variations show the presence of smaller dihedron imbricate into the main one. These results are validated by field observations. One seismic profile was carried out along the $E2$ electrical profile. We used 48 vertical geophones 3 m apart with a natural frequency of 4.5 Hz.

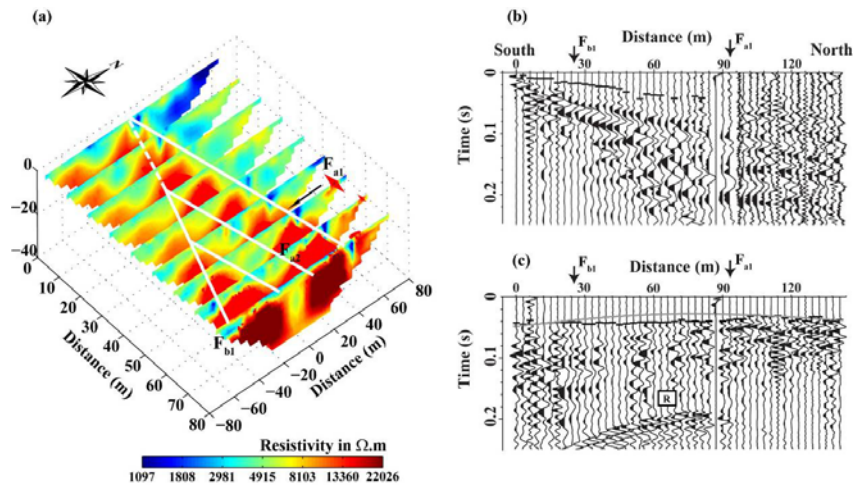


Figure 14. Geophysical investigation, (a) Block diagram showing the 9 electrical resistivity tomography profiles, with the surface at $14,000 \Omega.m$ and Seismic profile recorded for start (b) and fan shot (c). Black line represented picked first arrival and grey line theoretical time computed for a $N70^\circ$ fractured medium

Seismograms and first arrival picking are shown in Figure 14 for a start shot (b) and a fan shot (c). Figure 14b clearly shows a change of the wave field characteristics, as well as a strong decrease of the signal to noise ratio, at a distance of about 92 m, which corresponds to the trace of fracture F_{ai} . A more subtle modification of the signal frequency is observed at 26 m, close to the F_b trace. A fan shot was made at the dihedron edge (Figure 12c). P-waves exhibit a nearly constant arrival time (around 0.04 s), in spite of the distance variations (vertical black line in Figure 14c). The observed time values are compared in the same figure with theoretical times computed in a weak anisotropic medium ([THO 86]) characterized by a $N65^\circ$ oriented fracturing (vertical grey line in Figure 14c). P-waves are clearly delayed between the main fractures F_a and F_b , with a maximum value of about 0.01 s. These results highlight the fracturing effect within the tetrahedron, with a decrease of P-wave velocity. The extension of the tetrahedron is approximately delineated by the time anomaly.

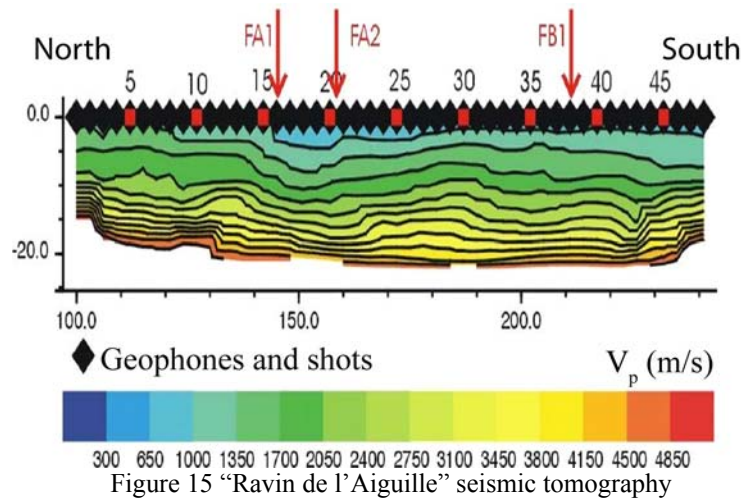


Figure 15 “Ravin de l’Aiguille” seismic tomography

The first arrival time of seismic waves have been pointed and inverted in order to obtain lateral and horizontal variation of P-Wave velocity. The use algorithm is SIRT ([DEM 00]). The obtained image (Figure 15) shows relative smooth velocity variation. In the centre of the profile, from geophone 15 to 36, we observe a very low velocity zone may be characterizing a highly fractured zone. Moreover, under the geophone 15, 21, 31 and 36, we can observe a lateral velocity gradient which could be indicate the presence of fracture. The fracture Fa_1 is located near the 16th geophone seem to confirm this observation.

Conclusion.

The seismic tomography, based on the inversion of first arrival of refracted wave with a geophone spacing of 3 m, has provided a smoothed seismic velocity images which do not allow a direct detection of fractures affecting the massif. However the two fractures limiting tetrahedron (Fa_1 and Fa_2) has been highlighted by a decrease of lateral seismic velocity and an increase of electrical resistivity within the dihedral tetrahedron. These results were associated with a higher degree of fracturing inside the tetrahedron. This interpretation was confirmed by the detailed analysis of seismic shooting and extreme range.

3.3 Cliff survey : Gorge de la Bourne

Geological context

The “Gorges de la Bourne” site is located in the Vercors massif, about 25 km south-west from Grenoble. The Cretaceous limestone cliff (Urgonian facies) is the consequence of Bourne river incision. The bedrock is slightly altered, as evidenced by a longitudinal seismic P-wave velocity measured at 6000 m/s on a 80 mm diameter rock sample and by a uniaxial compressive strength of 140 MPa [DEP 07]. It presents a porosity lower than 1% and low clay content.

The “Gorge de la Bourne” road, which was built between 1861 and 1872, is subject to frequent landslides and rockfalls. A dramatic collapse occurred on January 29 2004, which caused two deaths and the close of the road to circulation for more than one year, due to the high rock fall hazard. The observation of the scar showed that the fallen rock mass was bounded to the table part of the cliff by rock bridges, which represented only 5% of the total surface of the scar ([FRA 05], [FRA 09]). Few meters near the 2004 collapse, the road undercuts the cliff, forming a 2.5 m deep overhang under a slightly marked spur. A geological study highlights that subhorizontal bedding plane and vertical fracture undercut the rock mass. In particular, an open fracture was located four meters behind the cliff wall forming a potential rock fall hazard of 25 m high and 15 m large.

Geophysical investigation

In order to estimate the linear rock bridge percentage as well as the continuity of fractures observed from the wall, a geophysical study based on GPR system was performed. Two GPR multifrequency reflexions profiles (500 MHz and 800 MHz) and one Common Mid-Point (CMP) survey (200 MHz) were acquired with a RAMAC GPR system (Malå Geosciences). The locations of the profiles are displayed in Figure 16b. The 200, 500 and 800 MHz data were acquired using a sampling frequency of respectively 2000, 4000 and 5000 MHz, and during 420, 230 and 200 ns. All measurements were stacked 128 times in order to increase the signal to noise ratio.

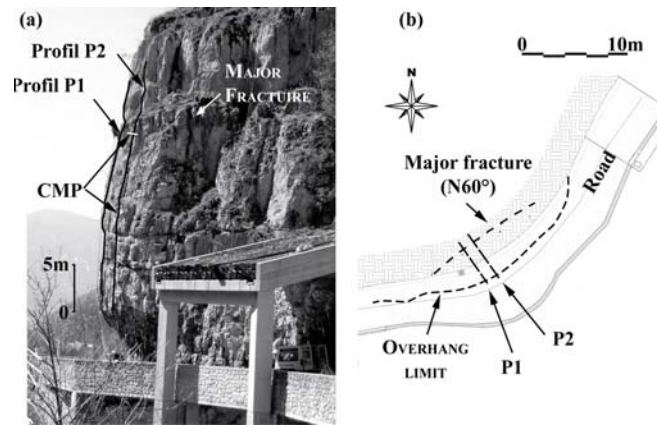


Figure 16. Photography of the investigated rock scale with locations of the two vertical profiles and limits of the CMP.

The processing and images were produced using Seismic Unix software ([STO 99]). The processing chain of raw data includes: i) DC removal (continuous current), zerophase band-pass filtering (depending of antenna frequency) and Automatic Gain Control (AGC) time equalization, followed by ii) static corrections of surface topography and time to depth conversion

The velocity used for time to depth conversion was derived from the Common Mid Point analysis [DEP 07]. The computed velocity profile shows a 1 m thick rock layer presenting a velocity around 9 cm/ns near the cliff face, followed by five 10cm/ns velocity layer within the rock mass. These values are compatible with limestone. The velocity contrast between the layers may be explained by the presence of less and more microfracture in each layer. Here, the higher amount of micro-fractures would be located within the first layer if their filling is clay or water (lower GPR velocity) or within the second one if their filling is air (higher GPR velocity).

Vertical Profile

Figure 17 present GPR images and their interpretation acquire along the cliff wall on the P1 and P2 profiles using the 500 MHz. For both profiles, penetration depth is around 6 meters for the 500 MHz antennas with a resolution of 5 cm. Resolution are estimated using the quarter of the GPR wavelength ([REY 97]).

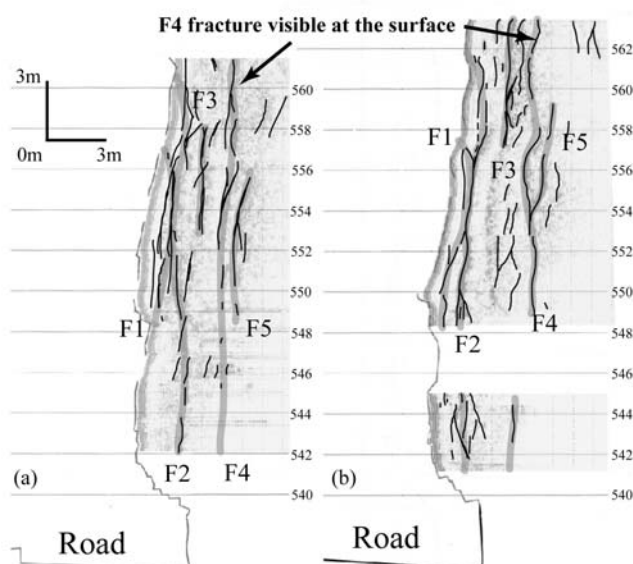


Figure 17. Gorge de la Bourne, Interpretation of P1 (a) and P2 (b) GPR profiles. Black thick lines represent the GPR fracture, grey line correspond to the interpreted structural model

Analysis of profiles 1 and 2 show five major fractures labelled F1 to F5. On the first two meters, two cracks are almost parallel to the cliff face (Fracture F1 and F2) which undercut the rock mass more and less continues. The F3 fracture is also almost parallel to the cliff face but is less persistent than fractures F1 and F2, especially between elevations 558 m and 560 m.

The large opening crack visible at the edge of the spur rock can be seen on both profiles (fracture F4), approximately four meters from the cliff wall. Finally, the deeper event F5 is located around five meters of depths. The last two fractures are well defined only in the upper part of the profile (between elevations 563 and 550 m). The fact that no reflected event was detected in the lower part (below 550 m) is an indication of the closing or vanishing of the fractures F4 and F5, i.e. they may be too thin to be detectable using these antennas or they may end at 550m elevation.

Discussion

The GPR acquisition makes it possible to determine the minimal extension of a fracture. Indeed, in order to show reflected events, a minimal aperture for a fracture is needed to be detected by GPR. This aperture is a function of the complex permittivity of the filling material in the fracture, the complex permittivity of the propagating medium and the frequency acquisition ([DEP 09]). Due to this

limitation, this method allows information on the minimal extension of the fractures and reciprocally, on the maximal extension of the rock bridges. This last parameters link the potentially unstable compartments to the stable rockmass.

In term of rock bridges, the maximal linear percentage reaches 8 and 10% respectively along P1 and P2 profiles for the F1 fracture, 6 and 8% respectively along P1 and P2 profiles for the F1 fracture. The fracture F3 and F4 present more than 20 % of rock bridges.

In terms of risk, the rock bridge percentage of the F1 and F2 fracture was considered too low to assume stability of the spur. From these results, the French government decided to mine the spur rock. The mining was performed inside the F4 crack, four meters from the cliff wall.

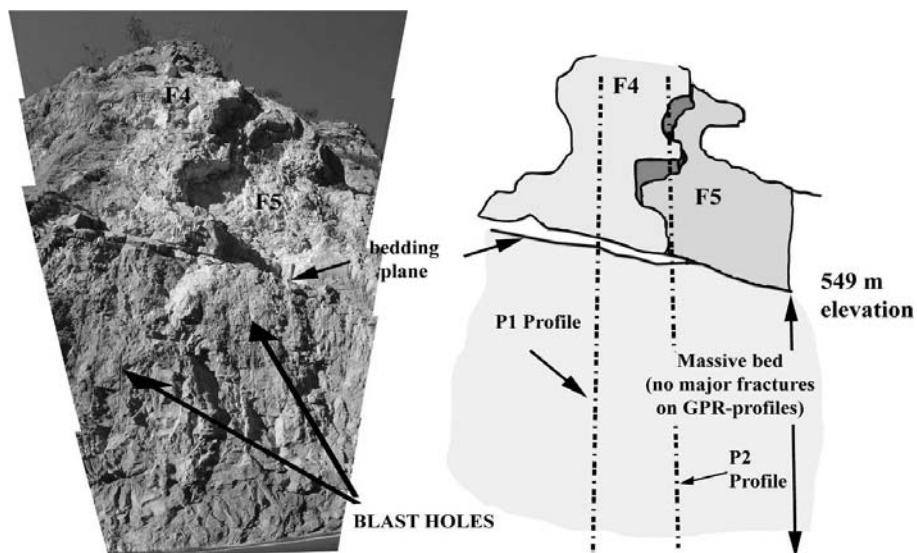


Figure 18. Photograph (a) and schema (b) of the rock scale after mining

Figure 18 displayed photography and the linked interpretation of the rock wall after mining. The surface which was exposed after mining appears in a light colour, in contrast to the patina which covers the surrounding rock surface. Above the elevation of 549 m, the surface corresponds to the pre-existing F4 and F5 fractures. Under the elevation of 549 m, where blast holes are visible, no pre-existing fracture

was opened by blasting, but a fresh fracture surface in the rock material was created. This observation confirmed the GPR images and the continuity of F4 fracture.

Conclusion

With these data, the local authorities decided to mine the rock slab in order to improve the safety of the road. This remediation technique was successfully used to compare the scars of fractures that were exposed after blasting with those deduced from the images obtained with GPR and with their continuity. The coherence between the spur after mining and the image shows the reliability of the GPR method.

3.3 Column survey: Chamousset

In this section, we use ambient seismic noise records to extract the resonance frequency of a prone-to-fall column and to evaluate its degree of coupling to the rock mass. The results presented here were obtained at the Chamousset site located in the South of the Vercors massif (western Alps, France) at an elevation of about 1900 m. Two prone-to-fall rock columns, 400 m apart and called Ch1 and Ch2, were identified at the top of the 300 m high east-facing cliff bordering the Vercors massif. This part of the cliff is made of near-horizontally meter-thick bedded Urgonian limestone. A structural study performed on the nearby outcrops located on the plateau showed that layers at the meter scale are affected by two near-vertical fracture sets striking N110-120°E and N30-50°E. At the hectometre scale, the mass is cut by N160° oriented near-vertical fracture planes which control the cliff orientation. The Ch1 column showed clear evidence of progressive opening of a 30 m long tension crack and fell down the 24 November 2007.

Digital Elevation Model (DEM) of the columns was obtained using Helicopter Lidar scans of the cliff (Figure 19, for details on Lidar methods, see chapter 2). For column Ch1, the cliff was scanned before and after the failure (Figure 19a and 1b), allowing the rupture plane to be delineated. This latter exhibits a complex shape, with two zones (in white in Figure 19b) showing evidence of fresh failures, which were interpreted as broken rock bridges. Column Ch1 (Figure 19a) was about 100 m high, 30 m wide and 2 m thick on the plateau, whereas column Ch2 is about 10 m wide and 4 m thick at its top with a height of about 30 m. Thus, the volume for Ch2, estimated to 2000 m³, is ten times less than the one of Ch1 (21,000 m³).

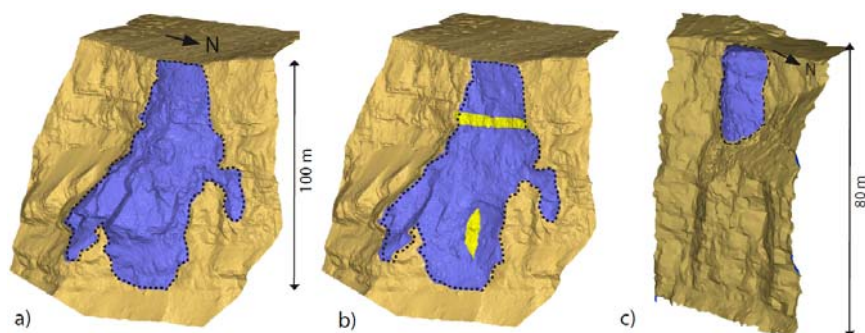


Figure 19. Digital Elevation Models of the cliff obtained from Helicopter Lidar acquisitions. Limits of the columns are in dashed lines. a) Ch1 site prior to its collapse. Rock column upper face is in blue. b) Ch1 site after the collapse. The broken plane is in blue and rock bridges zones are in yellow. c) Ch2 site prior to collapse.

Both columns were instrumented with seismometers at different periods. Ch1 site was equipped from July 2007 to November 2007 with one three-component 2 Hz geophone located on the plateau and one vertical sensor installed on the column. Unfortunately, this monitoring system ran out of order after heavy snow falls, on November 10, 2007, 14 days before the column collapse. Ch2 site was instrumented with two three-component 2Hz seismometers from mid-May 2009 to march 2010. One was located on the column while the other one was installed a few meters back on the plateau. Seismic noise windows of 5-s were extracted from the recorded data on both sites, with an anti-filtering STA/LTA ratio of 2 (with STA=0.5 s and LTA=20 s). Fourier spectra were calculated and summed to correspond to one hour of noise (e.g. 720 signal windows of 5 s). The noise amplitude on the Vercors plateau depends on several factors such as the wind speed and the rainfall. Therefore, we normalised each sum of spectra by its maximum in order to facilitate the comparison with time.

The spectra for the vertical sensor on column Ch1 (Figure 20a) clearly shows a dominant frequency around 3 Hz, which varies with time. This peak frequency probably corresponds to the column first natural frequency, as it has been checked by numerical modelling (section 2.5). It evolved from 3.6 Hz in July 2007 to 3.4 Hz at the beginning of October 2007. From that time to the 10th of November, it dropped to 2.6 Hz, 14 days before the collapse. Even if discontinuous, the natural frequency measurements allowed the decoupling of the column from the mass to be followed. Indeed, the column first natural frequency decreases with the breakage of rock bridges leading to the column failure, as it was evidenced by numerical modeling (section 2.5).

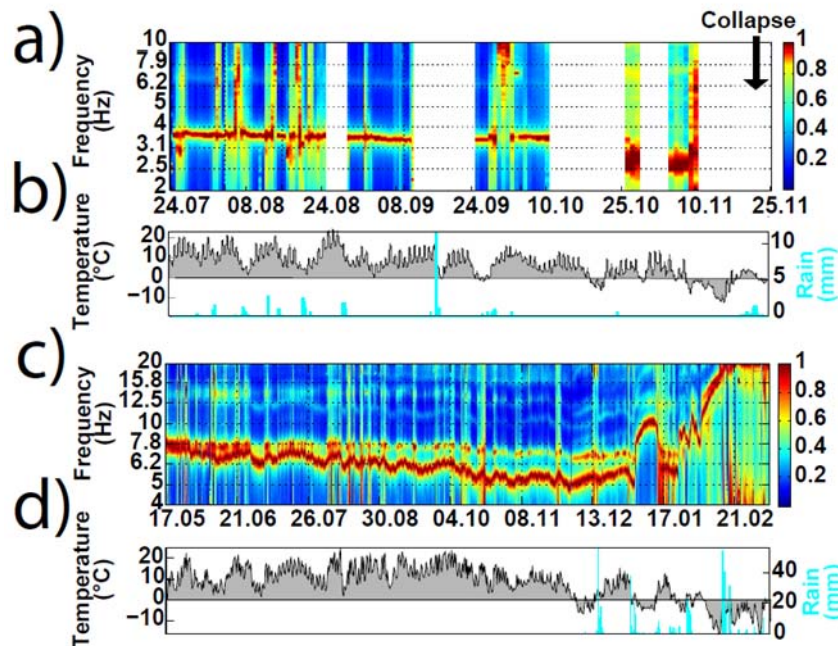


Figure 20 a) Evolution of normalized spectra (vertical component) with time on column Ch1, between the end of July 2007 to the 10th of November, 2007. The column collapse occurred on November 24 2007. b) Air temperature and rainfall data for the same period as in a). c) Normalized spectra on column Ch2, NW horizontal component, between the 17 May 2009 and the 24 February 2010 . d) Air temperature and rainfall data for the same period as in c).

Spectra calculated for the NW horizontal component on column Ch2 (Figure 20c) between mid-May 2009 and the end of February 2010 also show a dominant frequency around 6 Hz. This frequency, which was not observed on the rock mass spectra, was interpreted as the first natural frequency of column Ch2. Initially measured at 7.5 Hz in May 2009, it decreased with time to reach 5.5 Hz at the end of October 2009. The frequency rate drop is about 5% per month, which is lower than the frequency measured before the collapse of column Ch1. During that period, the normalised spectra curve exhibits oscillations, which were related to temperature variations (Figure 20b). In agreement with the smaller size of the column, the first natural frequency values are in a frequency range higher than those measured on column Ch1. At the end of 2009, this first natural frequency suddenly increased up to 25 Hz. This frequency augmentation was linked to the temperature drop below zero (compare Figure 20c and d) and rain falls, which generated development of ice

in the fracture. The consequence was the stiffening of the contact between the column and the rock mass. These data evidenced the link between the column natural frequency and the presence of rock and ice bridges. They show the interest of following this parameter for estimating rockfall hazard. It also raises the question of how to differentiate reversible variations of the first resonance frequency following the thermal seasonal effects from the irreversible variations of the first resonance frequency resulting from damaging (rupture of rock bridges). Another interesting feature of Ch2 spectra are the few other frequency peaks that can be seen in Figure 20c. They correspond to higher natural modes of Ch2 column, which are more easily observed when using three-component sensors. Indeed, resonance modes can vibrate along specific directions and their characterisation implies to measure the three components of the seismic motion.

In conclusions, it was shown that the column first natural frequency can be reliably and easily derived from seismic noise analysis, by computing the spectra of the vibrations measured at the column top. Measurements on the unstable rock column Ch1 evidenced that its first natural frequency decreased before its collapse, resulting from the breakage of rock bridges and the decay of the column-to-mass contact stiffness. Ambient noise records made during summer, fall and winter 2009 on the second column Ch2 showed that ice bridges could temporarily develop and dramatically increase the column natural frequency by stiffening the contact with the rock mass. Contrary to GPR performed on the cliff face, this technique offers the advantage to be operable from the top, avoiding the safety problems of abseiling. Based on seismic noise measurements and just requiring spectra computations, it could be easily incorporated in a monitoring system. Column-to-mass spectral ratios could also be computed to better detect the column resonance frequencies if two sensors are deployed. In the investigated sites, where columns were already significantly decoupled from the mass, spectra alone showed natural frequencies with enough accuracy. However, the use of this parameter as a precursor to rockfall requires setting apart reversible frequency variations due to thermal effects from the irreversible variations due to damaging. This can only be achieved by the simultaneous recording of weather parameters and needs a calibration period (whose duration depends on the site characteristics) in order to understand the influence of weather factors over the frequency variations. As an example, Ch2 first natural frequency appeared to be 10 times more sensitive to temperature fluctuations than Ch1 first natural frequency (1 Hz and 0.1 Hz for a 10°C change, respectively).

Conclusions

Characterizing the fracture pattern within steep rock slopes is of prime importance for fall hazard assessment. Three types of investigation techniques can be applied: direct field measurements, high resolution geophysical techniques and remote geodetic methods (laser scan and photogrammetry). Measuring slope fracturing is a complex problem, owing to the difficulty to perform structural measurements on near-vertical rock faces and to the lack of information on the persistence of fractures inside the mass. Remote geodetic techniques is increasingly used to solve the first problem (see the chapter XXX of this book). In some cases, geophysical techniques can be of use for determining the extent of fractures at depth. A review of three case studies considering various geophysical techniques was detailed to illustrate the potentialities of the geophysical techniques, whose applicability depends on the site characteristics.

The first site (Ravin de l'Aiguille) is an intensively fractured dihedron located at the top of a limestone cliff, which was too unsafe to abseil. All geophysical measurements had to be conducted on the plateau. Seismic and electrical imaging techniques were performed for mapping the fractures seen on the cliff. Only the ones with an opening larger than 1 m were detected using these methods, with a penetration limited to a few tens of meters. They however significantly contributed to delineate the geometry and the volume of the potential unstable block on this site.

The second site (Gorge de la Bourne) was an overhanging rock block of a few hundreds of m³ above a touristic road. For this site where abseiling was possible, GPR measurements performed on the cliff face provided detailed images of the fracture network, which were consistent with the observations made after mining the unstable block. When applied on cliff limestone face, the Ground Penetrating Radar (GPR) turned out to be the most effective method for imaging the fractures inside the mass. Resolution and penetration depth depend on the antenna frequency. The higher the frequency, the better the resolution and the lower the penetration are. In limestone, the maximum depth with 500 Mhz antenna was about 6 m for a resolution of a few cm. In more conductive geological formations (e.g in shale, micaschist or marly limestone), penetration depth can be much lower, owing to the attenuation of radar waves.

The two first case histories have shown that geophysical techniques offer interesting possibilities to image fractures in rock slopes, with however some limitations in terms of resolution and penetration. Another alternative proposed here is to measure an indirect but global parameter (resonance frequency) which varies with the coupling between the unstable block and the rock mass. On the third site (column of Chamouset) we have used the ambient seismic noise recorded by a seismic array for deriving the column natural frequencies, which evolves with its

degree of coupling to the rock mass. It has been shown the lowest resonance frequency is strongly controlled by the temperature and that irreversible damage can occur during freeze-thaw cycles and coincide with drops in resonance frequency, as the result of rock bridge breakage. This study suggests that seismic noise recording could be used for assessing the potential failure of unstable columns in rigid rocks.

Geophysical techniques cannot however be decoupled from geological and morphological observations, which are mandatory for understanding the mechanisms and interpreting geophysical data.

Acknowledgements

This research was partially funded by the French national RDT program (Ministère de l'Écologie et du Développement Durable). We thank Henry Mora for his help in adapting the GPR system to the cliff investigation. We thank the S.A.G.E (Société Alpine de Géotechnique) geotechnical company and Lyon CETE (Centre d'Études Techniques de l'Équipement) for help during geophysical acquisition. The experiment at Chamousset would not have been achieved without the help of the rangers of the Vercors Regional Park. It was partially funded by the A.N.R Triggerland, the federative structure V.O.R (Vulnérabilité des Ouvrages aux Risques) and the Marie Curie Program "Mountain Risks". The authors are also grateful to the "parc national Sismob (INSU-CNRS)" and the LGIT for the lending of instruments. The authors acknowledge Myotis society for collaboration in setting up the experiment.

References

- [ALB 04] ALBERTS C.P., "Surface reconstruction from scan paths. Future Generation Computer Systems", 20, 2004, 1285-1298.
- [AKI 02] AKI K., RICHARDS P., "Quantitative seismology", Univ Science Books, 2002.
- [ANN 02] ANNAN A., "Ground-penetrating radar workshop notes", in *Sensors and Software Inc.*, Ontario, Canada, 2002.
- [ARC 42] ARCHIE G.E., "The electrical resistivity log as an aid in determining some reservoir characteristics", *Petroleum Transactions of AIME* 146, 1942, 54-62.
- [BEN 95] BENSON A.K., "Application of ground penetrating radar in assessing 440 some geological hazards: examples of ground water contamination, faults, cavi.", *Journal of Applied Geophysics* 33, 1995, 177-193.
- [BON 06] BONNEFOY-CLAUDET S., COTTON F., BARD P.-Y., "The nature of noise wavefield and its applications for site effects studies", *A literature review, Earth-Science Reviews*, 79, 2006, 205 - 227.

- [BRA 06] BRADFORD J., DEEDS J., Ground-penetrating radar theory and application of thin-bed offset-dependent reflectivity: *Geophysics*, 71, no. 3, 2006, K47–K57.
- [BRU 59] BRUNE J., OLIVIER J., “The seismic noise of the earth's surface”, *Bulletin of the Seismological Society of America*, v. 49, no. 4, 1959, p. 349-353.
- [BUS 06] BUSBY J., JACKSON P., “The application of time-lapse azimuthal apparent resistivity measurements for the prediction of coastal cliff failure”, *Journal of Applied Geophysics*, 59, 2006, 261-272.
- [CAN 05] CANTIENI R., “Experimental methods used in system identification of civil engineering structures”, *Proceedings of 1st int operational modal analysis conference (IOMAC)*, Copenhagen, Denmark, 2005, 249–60.
- [CLI 06] CLINTON J. F., BRADFORD S. C., HEATON T. H., FAVELA J., “The Observed Wander of the Natural Frequencies in a Structure”, *Bulletin of the Seismological Society of America*, 96 n°1, 2006, 237–257.
- [DEM 00] DEMANET D., “Tomographies 2-D et 3-D à partir de mesures géophysiques en surface et en forage”, Ph. D. Thesis, Liege University, Belgium, 2000.
- [DEM 01] DEMANET D., RENARDY F., VANNESTE K., JONGMANS D., CAMELBEECK T., MEGHRAOUI M., “The use of geophysical prospecting for imaging active faults in the Roer Graben, Belgium”, *Geophysics* 66, 1, 2001, 78–89.
- [DEP 07] DEPARIS J., GARAMBOIS S., HANTZ D., “On the potential of ground penetrating radar to help rock fall hazard assessment: A case study of a limestone slab, Gorges de la Bourne French Alps”, *Engineering Geology*, 94, 2007, 89–102.
- [DEP 07b] DEPARIS J., “Etude des éboulements rocheux par méthodes géophysiques”, PhD thesis, Université Joseph Fourier, 2007.
- [DEP 08] DEPARIS J., FRICOUT B., JONGMANS D., VILLEMIN T., EFFENDIANTZ T., MATHY A., “Combined use of geophysical methods and remote techniques for characterizing the fracture network of a potentially unstable cliff site the “Roche du Midi,” Vercors massif, France” *Journal of Geophysics and Engineering*, 5, 2008, 147–157.
- [DEP 09] DEPARIS J., GARAMBOIS S., “On the use of dispersive APVO GPR curves for thin-bed properties estimation: Theory and application to fracture characterization”, *Geophysics*, 74, no. 1, 2009, J1-J12.
- [DEP 10] DEPARIS J., GARAMBOIS S., “Inversion Methodology of Dispersive Amplitude and Phase Versus Offset of GPR Curves (DAPVO) for Thin Beds”, in Miller, R.D., Bradford, J.H., Holliger, K., eds., *Advances in Near Surface Seismology and Ground-Penetrating Radar*, Society of Exploration Geophysicists, in press
- [DUS 03] DUSSAUGE-PEISSER C., WATHELET M., JONGMANS D., HANTZ D., COUTURIER B., SINTES, M., “Seismic tomography and ground penetrating radar applied on fracture characterisation in a limestone cliff, Chartreuse massif, France”, *Near Surface Geophysics*, 1, 2003, 161-172.

- [FRA 05] FRAYSSINES M., “Contribution à l'évaluation de l'aléa éboulement rocheux (rupture)”, PhD thesis, Université Joseph Fourier, 2005.
- [FRA 06] FRAYSSINES M., HANTZ D., “Failure mechanisms and triggering factors in calcareous cliffs of the subalpine ranges (french alps)”, *Engineering Geology* 86, 2006, 256–270.
- [FRA 09] FRAYSSINES M., HANTZ D., “Modelling and back analysing failures in steep limestone cliffs”, *International Journal of Rock Mechanics & Mining Sciences* 46, 2009 1115–1123.
- [GRA 96] GRASMUECK M., “3-d ground penetrating radar applied to fracture imaging in gneiss”, *Geophysics* 61, 1996, 1050–1064.
- [GRA 05] GRASMUECK M., WEGER R., HORSTMAYER H., “Full-resolution 3d gpr imaging”, *Geophysics*, 70, 2005, K12–K19.
- [GRE 04] GRÉGOIRE C., HOLLENDER F., “Discontinuity characterization of the spectral content of ground penetrating radar (GPR) reflections — Application of the Jonscher model”, *Geophysics*, 69, 2004, 1414–1424.
- [HAC 00] HACK R., “Geophysics for slope stability”, *Surveys of Geophysics*, 21, 2000, 423–448.
- [HAV 04] HAVSKOV J., ALGUACIL G., “Instrumentation in Earthquake Seismology”, Springer, 358 pp, 2004.
- [HEI 06] HEINCKE B., MAURER H., GREEN A.G., WILLENBERG H., SPILLMANN T., BURLINI L., “Characterizing an unstable mountain slope using shallow 2- and 3-d seismic tomography”, *Geophysics*, 71, 2006, B241-B256.
- [HEI 10] HEINCKE B., GÜNTHER T., DALSEGG E., RØNNING J.S., GANERØD G.V., ELVEBAKK H., “Combined three-dimensional electric and seismic tomography study on the Åknes rockslide in western Norway”, *Journal of Applied Geophysics* 70, 2010, 292–306
- [HOE 81] HOEK E., BRAY J., “Rock slope engineering (revised third edition)”, Institution of Mining and Metallurgy, London, 1981.
- [HUM 90] HUMAR J.L., “Dynamics of structures,” Prentice-Halls, 780p, 1990.
- [JEA 06] JEANNIN M., GARAMBOIS S., JONGMANS D., GREGOIRE C., “Multiconfiguration gpr measurements for geometric fracture characterization in limestone cliffs (alps)”, *Geophysics*, 71, 2006, B85-B92.
- [JON 00] JONGMANS D., HEMROULLE P., DEMANET F., RENARDY F., VANBARANT Y., “Application of 2D electrical and seismic tomography techniques for investigating landslides”, *European Journal of Environmental and Engineering Geophysics* 5, 2000, 75–89.
- [JON 07] JONGMANS D., GARAMBOIS S., “Surface geophysical characterization and monitoring : a review”, *Bull. Soc. Géol. France*, 178, 2007, 101-112.

- [KEA 02] KEAREY P., BROOKS M., HILL I., “An Introduction to Geophysical Exploration. 3rd edition” – Blackwell, Oxford, 262 pp, 2002.
- [LAN 00] LANE J. W., BUURSINK M. L., HAENI F. P., VERSTEEG R. J., “Evaluation of ground-penetrating radar to detect free-phase hydrocarbons in fractured rocks—results of numerical modeling and physical experiments”, *Ground Water*, 38, 2000, 929–93.
- [LAN 98] LANZ E., MAURER H. R., GREEN A. G., “Refraction tomography over a buried waste disposal site”, *Geophysics*, 63, 1998, 1414–1433.
- [LEV 10] LÉVY C., BAILLET L., JONGMANS D., MOUROT P., HANTZ D., “Dynamic response of the Chamousset rock column (Western Alps, France)”, *J. Geophys. Res.*, 115, 2010.
- [LOK 96] LOKE M.H., BARKER, R.D., “Rapid least-squares inversion of apparent resistivity pseudosections by a quasi-Newton method”, *Geophysical Prospecting*, 44, 1996, 131-152.
- [MAT 98] MATSUMOTO M., NISHIMURA T., MERSENNE T., “A 623-dimensionally equidistributed uniform pseudorandom number generator”, *ACM Trans. on Modeling and Computer Simulation*, 8 (1), 1998, 3–30.
- [MAV 95] MAVKO G., MUKERJI T., GODFREY N., “Predicting stress-induced velocity anisotropy in rocks”, *Geophysics*, 60, 1995, 1081–1087.
- [MCC 90] MCCANN D., A. Foster, “Reconnaissance geophysical methods in landslide investigations”, *Engineering Geology* 29, 1990, 59–78.
- [NOR 09] NORDVIK T., GRØNENG G., GANERØD G., NILSEN B., HARDING C., BLIKRA L., “Geovisualization, geometric modeling and volume estimation of the Åknes rockslide, Western Norway”, *Bulletin of Engineering Geology and the Environment* 68, 2009, 367–384.
- [PET 96] PETTINELLI E., BEAUBIEN S., TOMMASI P., “Gpr investigation to evaluate the geometry of rock slides and buckling in a limestone formation in northern Italy”, *European Journal of Environmental and Engineering Geophysics* 1, 1996, 271–286.
- [PIP 03] PIPAN M., FORTE E., GUANGYOU F., FINETTI I., “High-resolution gpr imaging and joint characterisation in limestones”, *Near Surface Geophysics* 1, 2003, 39–55.
- [RAS 03] RASHED M., KAWAMURA D., NEMOTO H., MIYATA T., NAKAGAWA K., “Ground penetrating radar investigations across the Uemachi Fault, Osaka, Japan”, *Journal of Applied Geophysics* 53, 2003, 63–75.
- [REN 04] REN W.X., ZHAO T., HARIK I.E., M.ASCE, “Experimental and Analytical Modal Analysis of Steel Arch Bridge”, *Journal of Structural Engineering*, 2004, pp.1022-1031.
- [REY 97] REYNOLDS J.M., “An introduction to applied and environmental geophysics”, John Wiley & Sons, Chichester, England, 806pp, 1997.

- [ROC 06] ROCH KH., CHWATAL E., BRÜCKL E., “Potential of monitoring rock fall hazards by GPR : considering as example of the results of Salzburg”, *Landslide*, 3, 2006, 87-94.
- [SAN 01] SANTAMARINA J.C., KLEIN K., FAM M., “Soils and waves”. John Wiley & Sons, Chichester, UK, 508pp, 2001.
- [SHA 97] SHARMA P.V., “Environmental and Engineering Geophysics”, Cambridge University Press, 1997.
- [STE 95] STEVENS K.M., LODHA G.S., HOLLOWAY A.L., SOONAWALA N.M., “The application of ground penetrating radar for mapping fractures in plutonic rocks within the Whiteshell Research Area, Pinawa, Manitoba, Canada”, *Journal of Applied Geophysics* 33, 1995, 125–141.
- [STO 99] STOCKWELL J.W., “The cwp/su: seismic unix package”, *Computers & Geosciences*, 25, 1999, 415–419.
- [TEL 90] TELFORD W.M.; GELDART L.P., SHERIFF, R.E., “Applied Geophysics (2nd Edition)”, Cambridge University Press, 1990.
- [THO 86] THOMSEN L., “Weak elastic anisotropy”, *Geophysics*, 51, 1986, 1954-1966.
- [TOS 95] TOSHIOKA T., TSUCHIDA T., SASAHARA K., “Application of GPR to detecting and mapping cracks in rock slopes”, *Journal of Applied Geophysics* 33, 1995, pp. 119–124.
- [YOU 96] YOUNG C.J., CHAEL E.P., WITHERS M.M., ASTER R.C., “A comparison of the high-frequency (>1 Hz) surface and subsurface noise environment at three sites in the United States”, *Bulletin of the Seismological Society of America*, vol. 86, no. 5, 1996, p. 1516-1528.
- [ZOU 01] ZOU D. H., WU Y. K., “Investigation of blast-induced fracture in rock mass using reversed vertical seismic profiling”, *Journal of Applied Geophysics*, 48(3), 153, 2001?